Journal Pre-proof

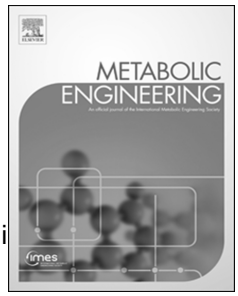

Metabolic flux and resource balance in the oleaginous yeast *Rhodotorula toruloides*

Eric J. Mooney, Patrick F. Suthers, Wheaton L. Schroeder, Hoang V. Dinh, Xi Li, Yihui Shen, Tianxia Xiao, Catherine M. Call, Heide Baron, Arjuna M. Subramanian, Daniel R. Weilandt, Felix C. Keber, Martin Wühr, Joshua D. Rabinowitz, Costas D. Maranas

PII: S1096-7176(25)00185-5

DOI: https://doi.org/10.1016/j.ymben.2025.11.012

Reference: YMBEN 2419

To appear in: *Metabolic Engineering*

Received Date: 12 August 2025

Revised Date: 18 October 2025

Accepted Date: 16 November 2025

Please cite this article as: Mooney, E.J., Suthers, P.F., Schroeder, W.L., Dinh, H.V., Li, X., Shen, Y., Xiao, T., Call, C.M., Baron, H., Subramanian, A.M., Weilandt, D.R., Keber, F.C., Wühr, M., Rabinowitz, J.D., Maranas, C.D., Metabolic flux and resource balance in the oleaginous yeast *Rhodotorula toruloides*, *Metabolic Engineering*, https://doi.org/10.1016/j.ymben.2025.11.012.

Metabolic flux and resource balance in the oleaginous yeast *Rhodotorula toruloides*

Eric J. Mooney[a,b], Patrick F. Suthers[b,c], Wheaton L. Schroeder[c,d], Hoang V. Dinh[b,c], Xi Li[e,f,g], Yihui Shen[f,g,i], Tianxia Xiao[f,g,h], Catherine M. Call[f,g,j], Heide Baron[f,g], Arjuna M. Subramanian[f,g], Daniel R. Weilandt[e,f,g,l], Felix C. Keber[f,g], Martin Wühr[g,k], Joshua D. Rabinowitz[e,f,g,l], Costas D. Maranas[b,c]*

a. Department of Biochemistry and Molecular Biology, The Pennsylvania State University, University Park, PA, 16802, USA
b. DOE Center for Advanced Bioenergy and Bioproducts Innovation, The Pennsylvania State University, University Park, PA, 16802, USA
c. Department of Chemical Engineering, The Pennsylvania State University, University Park, PA, 16802, USA
d. Gene and Linda Voiland School of Chemical Engineering and Bioengineering, Washington State University, Pullman, WA, 99164, USA
e. DOE Center for Advanced Bioenergy and Bioproducts Innovation, Princeton University, Princeton, NJ, USA
f. Department of Chemistry, Princeton University, Princeton, NJ, USA
g. Lewis-Sigler Institute for Integrative Genomics, Princeton University, Princeton, NJ, USA
h. Current address: State Key Laboratory of Female Fertility Promotion, Beijing Key Laboratory of Reproductive Endocrinology and Assisted Reproductive Technology, Center for Reproductive Medicine, Department of Obstetrics and Gynecology, Peking University Third Hospital, Beijing, China
i. Current address: Department of Bioengineering, University of Pennsylvania, Philadelphia, PA 19104, USA
j. Brown University Department of Orthopaedic Surgery, Providence, RI 02912, USA

k. Department of Molecular Biology, Princeton University, Princeton, NJ 08544, USA

l. Ludwig Institute for Cancer Research, Princeton Branch, Princeton, NJ, USA

* Correspondence: costas@psu.edu

Abstract

The yeast *Rhodotorula toruloides* is a promising bioproduction organism due to its high lipid yields and ability to grow on cheap and abundant substrates. Quantitative, systems-level assessment of its metabolic activity is accordingly merited. Resource-balance analysis (RBA) models capture not only reaction stoichiometry but also enzyme requirements for catalysis, providing valuable tools for understanding metabolic trade-offs and optimizing metabolic engineering strategies. Here, we present systems-level measurements of *R. toruloides* metabolic flux based on isotope tracing and metabolic flux analysis. In combination with new proteomic measurements, these flux data are used to parameterize a genome-scale resource balance model rtRBA. We find that *S. cerevisiae* and *R. toruloides* grow at nearly indistinguishable rates using similar biosynthetic but dramatically different central metabolic programs. *R. toruloides* consumes one-fifth as much glucose, which it metabolizes primarily via the pentose phosphate pathway and TCA cycle unlike primarily glycolysis in *S. cerevisiae.* Overall, across these two divergent yeasts, protein abundances aligned more closely than metabolic flux. Resource balance modeling of these metabolic programs predicts superior theoretical yields but lower productivities in *R. toruloides* than *S. cerevisiae* for industrial chemicals, highlighting the value of rapid glucose uptake for productivity but respiratory metabolism for yields.

1 Introduction

Fossil fuels are still the world's main energy source (IEA, 2021) and major precursors to many compounds, with millions of tons converted annually into fertilizers, plastics, and more (Levi and

Cullen, 2018). Global dependence on these nonrenewable resources could be reduced by using oils made from yeasts as partial replacements, particularly for fuels and detergents (Liu et al., 2021). However, low yields and high extraction costs for bio-produced oil from yeasts have thus far prevented them from becoming cost-competitive with fossil fuels (Bandhu et al., 2020; Zainuddin et al., 2021). Cost-cutting measures such as growing yeasts on cheap and abundant carbon sources, including lignocellulosic plant biomass (LPB) from crop residues, can improve cost-competitiveness (Koh et al., 2024). However, LPB contains a heterogeneous mix of carbon substrates with inhibitory compounds that commonly used industrial yeasts such as *Saccharomyces cerevisiae* (SC) cannot natively utilize or tolerate. Likewise, *Yarrowia lipolytica*, another oleaginous yeast considered for industrial lipid production, cannot reliably use xylose – one of the two main sugars in LPB (Sànchez Nogué and Karhumaa, 2015) – as a carbon source (Li and Alper, 2016). In contrast, *Rhodotorula toruloides* (RT) can readily convert LPB into fuels, including fatty alcohols and bisabolene (Liu et al., 2021), and has a wider carbon substrate utilization and increased tolerance to inhibitory compounds than SC. When inserting a fatty acyl-CoA reductase from *Marinobacter aquaeolei* VT8, the primary fatty alcohols produced *in vivo* (and thus the ones RT is best suited to producing industrially) are oleic, stearic, and cetyl alcohol (Fillet et al., 2015). RT also synthesizes carotenoids, hence its characteristic red color, providing a less energy-intensive alternative to the chemical synthesis of cosmetic pigments and a source of antioxidants for soaps (Ribeiro et al., 2023). Thus, RT is a promising candidate for the conversion of LPB to fatty acids as precursors to fuels and detergents. Most lipids produced by RT are triacylglycerols (TAGs) (Tiukova et al., 2019a), a potential biodiesel precursor (Palmer and Brigham, 2016). RT has also been explored for the production of bisabolene (Liu et al., 2021), fatty alcohols (Fillet et al., 2015), and TAGs (Tiukova et al., 2019a). Here we use metabolic

71 modeling to pinpoint stoichiometric and proteomic bottlenecks and explore engineering strategies
72 to further boost achievable yields and titers using RT.

73 Widespread adoption of RT as a widely used biofuel and lipid producer requires further
74 reengineering guided by a better understanding of its metabolism (Zhang et al., 2021) to overcome
75 barriers. For instance, it is unclear why RT does not make ethanol under laboratory conditions
76 despite prior reports that RT possesses the required genes (Zhu et al., 2012) and that the necessary
77 proteins for converting pyruvate to ethanol are expressed when grown in batch conditions (Li et
78 al., 2025). In contrast to RT, SC uses glycolysis and produces ethanol even when glucose and
79 oxygen are abundant (i.e., the Crabtree effect) (C. Verduyn, 1984). Modeling efforts have
80 suggested that this phenotype in SC is driven by limitations in mitochondrial and ribosomal
81 capacity (Dinh and Maranas, 2023; Shen et al., 2024). In contrast, recent quantitative experiments
82 suggest that high expression of glycolytic enzymes in SC, which render SC prepared for potential
83 future anoxia, may be the primary factor (Shen et al., 2024).

84 Genome-scale metabolic (GSM) models (Thiele and Palsson, 2010) have been widely used
85 to predict growth phenotypes under different conditions (O'Brien et al., 2013), find genetic targets
86 for metabolic engineering (Burgard et al., 2003; Gu et al., 2019), and uncover essential genes and
87 gene pairs (Burgard et al., 2016; Trinh et al., 2008) among many other uses. GSM models facilitate
88 faster and less costly exploration of the strain design spaces than relying solely on *in vivo* testing.
89 Model-based insight can be used to not only find non-intuitive solutions for improving yields (Kim
90 et al., 2019) but also filter out at an early stage non-viable concepts. Some notable and successful
91 use cases include improving ethanol and 1,4-butanediol yields from *E. coli* (Dinh et al., 2019) and
92 predicting genes to overexpress in the yeast *Komagataella phaffii* for improving *S*-adenosyl-L-
93 methionine production (Subash Chandra Bose et al., 2023). Curated GSM models based on growth

phenotyping and multi-omics datasets have recently been published for the RT strain NBRC 0880, such as *iRhto*1108 (Dinh et al., 2019), rhto-GEM (Tiukova et al., 2019b), and Rt_IFO0880 (Kim et al., 2020). These GSM models have successfully recapitulated proven metabolic engineering strategies for improving TAG yields (Dinh et al., 2019; Kim et al., 2020) as well as correctly predicted the essentiality of hundreds of genes (Dinh et al., 2019; Kim et al., 2020). These GSM models can thus serve as *in silico* blueprints for exploring lipid production and probing RT's capabilities as a bio producer.

However, as GSM models do not directly link fluxes to the production and turnover rates of their requisite enzymes or transporters, they are often overly optimistic and cannot capture bottlenecks associated with inefficient turnover or limited ribosomal capacity (Goelzer et al., 2015). For RT, inefficient sugar transporters have been suggested as the main bottleneck on lipid yields from plant biomass (Tiukova et al., 2019a). Furthermore, stifled shuttling of acetyl-CoA from the mitochondria to the cytoplasm where carotenoid-producing pathways are concentrated, has been proposed as an obstacle to improving carotenoid production (Xie et al., 2024). In both cases, it is unclear whether the cost of producing these transporters or limitations of membrane surface area could be the key limitations.

One modeling approach that assesses how protein production costs affect reaction fluxes is resource balance analysis (RBA) (Goelzer et al., 2011; Goelzer et al., 2015). Briefly, in RBA, fluxes are limited by the *in vivo* apparent turnover number (k_{app}) of their associated enzymes or transporters and the rates at which they can be produced (Dinh and Maranas, 2023). Enzyme production rates depend on their protein compositions, their component sequences, ribosome translation capacity, ribosome abundance, and availability of requisite cofactors. RBA models can be used to assess transportation bottlenecks in terms of proteome allocation and contrast alternative

117 modifications such as adding transporters from other species or designing new ones that are faster
118 or less resource intensive. Their ribosome constraints and reliance on proteomics data to infer
119 enzyme demands complement the homology-based approach taken by a model of another RT
120 strain (Rekena et al., 2023), providing parameters that are more sensitive to specific experimental
121 conditions at the expense of being less generalizable. Furthermore, a recent review article
122 (Schroeder et al., 2024) compared several metabolic modeling frameworks that require
123 macromolecule synthesis, and found RBA to be the most data-tractable of these frameworks "for
124 non-model organisms". This results partly from the RBA framework having the lowest data
125 requirements among the frameworks compared, as well as some automated tools to make
126 reconstruction more convenient.

127 Our study of RT addresses the following questions. First, how does RT's proteome allocation
128 compare to SC's, and does this help explain any known differences between both yeasts or reveal
129 new ones? Second, how do observed yields compare to maximum theorical yields (MTYs)
130 predicted by FBA and RBA of TAGs and fatty alcohols?

131 In this study, we introduce protein and ribosomal cost constraints into *iRhto*1108 to create an
132 RBA model of RT, named rtRBA1266 (henceforth referred to as rtRBA). Specific derived versions
133 were made for batch conditions (i.e., rtRBA-B) as well as chemostats under carbon and nitrogen
134 limitation, named rtRBA-C-1 and rtRBA-N-1 respectively (i.e., version 1 of rtRBA-C and rtRBA-
135 N). This process was accomplished largely using the scRBA model's development pipeline and
136 framework (Dinh and Maranas, 2023), which we revised to be more flexible and incorporate other
137 adjustments, such as supporting heterogeneous ribosome compositions, and allowing models to be
138 parameterized to fit *in vivo* flux ranges. Proteomics data was collected and used to parameterize *in*
139 *vivo* turnover numbers, adjust ATP maintenance (ATPM) demands, and develop constraints on the

mitochondrial proteome capacity. Using metabolic flux analysis (MFA), flux estimates were obtained based on ^{13}C labeling experiments. To better account for how fluxes are impacted by the protein and cofactor production demands reflected by RBA, the RBA model calculated its own fluxes that matched the MFA fluxes as closely as possible, which were then used to determine k_{app} values. We then applied this updated RBA framework to scRBA to better compare the capabilities of RT and SC; this new scRBA version can be found at https://github.com/EarthToMooney/scRBA.

2 Methods

2.1 GSM model updates

The version of the GSM model *iRhto*1108 simulating carbon-limited growth (available at https://github.com/maranasgroup/iRhto_memote), referred to here as *iRhto*1108C, was updated with new genes, metabolites, and reactions (see Supplementary Text 1 for details) (Dinh et al., 2019). Annotations were updated where appropriate, such as including EC 7.1.1.8 alongside its older version (i.e., EC 1.10.2.2). This updated GSM model for RT is henceforth referred to as *iRhto*1120. Modifications include updating gene-protein-reaction (GPR) associations to include three genes omitted from *iRhto*1108 (LOT6, GRX1 and COQ4) that have homologs (identified via UniProt annotations) present in GPRs from *iSace*1144, which is the GSM model associated with scRBA (Dinh and Maranas, 2023). Both carbon- and nitrogen- limited variants of *iRhto*1120, along with details about model curation, are recorded in Supplementary Text 1 and at https://github.com/maranasgroup/rtRBA/tree/main/build_model/input. *iRhto*1120 contains 2,066 metabolites, 1,985 of which are from *iRhto*1108. Nine metabolites involved in no reactions from *iRhto*1108 were assessed; one (5-formyltetrahydrofolic acid in the mitochondria) was addressed

by adding an annotation-supported reaction (tetrahydrofolate aminomethyltransferase), while the other 8 metabolites were removed since no evidence was found for their inclusion.

2.2 RBA model reconstruction

We generally followed the procedure used to reconstruct the scRBA model (Dinh and Maranas, 2023) when reconstructing the RBA model rtRBA; Supplementary Figure 1 summarizes our workflow. Specifically, the formulation for enzyme and ribosome production – along with updated versions of the underlying code and constraints forming rtRBA – were adapted from scRBA's reconstruction workflow (Dinh and Maranas, 2023). The resulting model is available in the Supplementary Materials and on GitHub at https://github.com/maranasgroup/rtRBA.

During the update of the GSM model for use in rtRBA, 50 new pseudo-reactions were added to allow proteins with multiple possible cofactors to use all available options (e.g., making proteins which can use Fe^{2+} or Fe^{3+} as cofactors now consumes a generic "FeCATION" cofactor which can be made irreversibly from either ion). These were done to reduce the duplication of protein synthesis with multiple viable cofactors.

Ribosome composition was determined via annotations from the latest annotated genome of RT (v4.0, GenBank accession LCTV00000000) (Coradetti et al., 2018). The roles of all ribosome components were further verified by BLASTn and BLASTp searches (Altschul et al., 1990) against rRNA sequences for RT from RNAcentral (Consortium, 2021) and the ribosomal proteins used in SC, respectively. To account for paralogs (interchangeable ribosomal proteins) of each subunit when performing gene knockout simulations, paralogs are converted into a generic subunit named after the first protein listed in each paralog set. For example, RPL14A and RPL14B form a generic subunit (named RIBOSUB-RPL14A in the model). The experimentally determined ribosome efficiency constant (k_{ribo}) of 6.6 amino acids/ribosome/s (Rekena et al., 2023) was used

as an initial estimate for the rate of translation elongation. Since growth remained infeasible at the highest measured rate (0.38 h^{-1}) under glucose-fed batch conditions, the value was increased by 0.1 until growth could be recapitulated, as was done for scRBA (Dinh and Maranas, 2023). This resulted in k_{ribo} values of 14.2 and 12.2 amino acids/ribosome/s for the cytosolic and mitochondrial ribosomes, respectively. Their scRBA counterparts were both set to 13.2 in its original release (Dinh and Maranas, 2023) but were adjusted to 13.6 when fitting the model to the proteomics and MFA data processed for the current work.

The rate of ribosome production constrains the translation rates of proteins (i.e., ribosome-protein coupling and rRNA capacity constraints), which in turn limits the production fluxes of transporters and enzymes. Enzyme compositions and subcellular localizations were determined from the UniProt entries associated with proteins from the annotated genome (i.e., Proteome UP000239560) (Coradetti et al., 2018). The total fraction of proteins that can reside in or on the mitochondria (as determined by their subcellular compartments in the GSM model) was found to comprise no more than 14.0% of the cell's proteome by mass. This mass fraction of the proteome was used as an upper limit on the total mass of the model's proteins located in and on the mitochondria, to reflect their smaller volumes and membrane surface areas.

To account for a protein's usage as a subunit (e.g., for transporters or enzymes) and in the biomass reaction, each translation reaction makes one protein copy and an amount of protein mass equal to that protein's molecular weight. Depending on the protein, each protein copy can be an enzyme, ribosomal subunit or carry out a non-metabolic function that is not captured by the RBA model. For the latter, in the RBA model an artificial sink reaction is appended (referred to as "protein wasting" in scRBA). In the original release of scRBA, however, proteins not involved in

transport or metabolic processes lacked translation reactions and were aggregated into a so-called "dummy" protein using an average amino acid composition (Dinh and Maranas, 2023).

In rtRBA and our updated scRBA version, however, measured and unmeasured proteins in this cohort are treated differently. All measured proteins (i.e., have proteomics data) were added to the model, including those not already present through GPR associations, and thus must be translated by the cytosolic ribosome unless evidence was found to suggest otherwise (e.g., being encoded by mtDNA). In the glucose-fed batch cultures that are simulated in this study, less than 1% of the proteome's mass has not been identified, possibly stemming from measurement error or proteins that could not be identified. To account for this unidentified fraction of the proteome during k_{app} calculations, we allow it to be filled by unmeasured proteins. Because the unidentified fraction was so small, and thus may be impacted heavily by measurement error, we allow the translation fluxes of measured proteins to deviate by as much as 1% from their measured values (for specific details, see the description of slack variables in Supplementary Text 1, Section E).

When comparing yields and k_{app} values between scRBA and rtRBA, the updated RBA protocol used in rtRBA was retroactively applied to scRBA to ensure consistency, with other checks performed to compare the original and revised scRBA models. This included adding all measured proteins to the model to allow more accurate fitting to proteomics data, resulting in 4,961 new proteins in scRBA. Furthermore, this introduced the option to assign proteins to be translated by any ribosome, which was only used to aid in testing k_{app} calculations using proteomics and fluxomics data from (Shen et al., 2024). These calculations initially could not recapitulate the measured growth rate when allowing only the cytosolic ribosome to translate the newly added proteins but did so successfully after also allowing the mitoribosome to translate them, thus suggesting that some proteins were assigned to the wrong ribosome. We assigned six more proteins

to the mitoribosome since they are encoded in mtDNA, bringing the total number of mitoribosome-translated proteins in scRBA to 13. These include mitochondrial ATP synthase subunit 9, along with five newly added proteins: DNA endonuclease aI4, RNA maturase bI4, putative COX1/OXI3, putative COX1/OXI3, and DNA endonuclease aI5 alpha (see Supplementary Text 1 for full list). All other proteins were restricted to the cytosolic ribosome. Upon updating the k_{ribo} parameter value for the cytosolic and mitochondrial ribosome from 13.2 amino acids/ribosome/s to 13.6, the feasibility of the RBA calculations was restored.

As in scRBA, reactions from a GSM model are split into separate versions for each enzyme or transporter that facilitates them, as well as a spontaneous version, if indicated. If a reaction is reversible, it is divided further into forward and reverse versions. Dividing reactions into these separate versions (henceforth referred to as just "reactions" unless otherwise specified) enables allowing further customization of k_{app} values, as well as simplifying minimization of total fluxes during k_{app} calculations.

2.3 Protein abundance measurements, atom mapping model, and metabolic flux analysis

We followed the procedure from Shen et al. (2024) for protein abundance measurements, ^{13}C labeling data collection, atom mapping model (AMM) construction, and MFA. Briefly, ^{13}C labeling data and biomass composition were collected for RT at a growth rate of 0.38 h^{-1} under the same glucose-fed batch conditions as SC (i.e., minimal media, yeast nitrogen base without amino acids). The AMM and labeling data were then incorporated into MFA simulations using a prior formulation (Gopalakrishnan and Maranas, 2015). The AMM, input data, biomass composition worksheet, MFA evaluation, and additional annotations are available at https://github.com/maranasgroup/yeastsMFA.

252 To develop our AMM, flux variability analysis (Mahadevan and Schilling, 2003) was
253 performed with constraints derived from experimental glucose uptake to remove reactions
254 incapable of carrying flux under glucose utilizing conditions, such as degradation pathways that
255 form ATP-consuming futile cycles with biosynthesis of nucleotide, lipid, fatty acid, and
256 carbohydrates. We noted that there was no byproduct secretion observed. We also simplified
257 intracellular compartments by assigning non-mitochondrial reactions to the cytosol. Carbon
258 mapping of reactions were obtained from a previous large-scale mapping model in *E. coli*
259 (Gopalakrishnan and Maranas, 2015), or for new reactions curated from the BioCyc database
260 (Caspi et al., 2016), biochemistry textbooks, and the literature. Annotation of functional groups
261 and adjacent carbon atoms were also provided for carbon atoms (which were previously associated
262 with only numbering indexes) (see
263 https://github.com/maranasgroup/yeastsMFA/tree/master/resources). The model also reflects
264 cofactor usage (e.g., ATP and NADH), as well as proton pumping and the electron transport chain
265 pathway. Stoichiometry of the 52 precursors in the biomass reactions are updated to reflect
266 condition-specific macromolecular composition measured in this study. The mapping model
267 contains 373 reactions and 348 metabolites.

268 For external flux and growth rate measurement, RT was first grown overnight in yeast
269 nitrogen base medium without amino acids (YNB, Sigma-Aldrich, Y0626) consisting of 0.2%
270 glucose and then inoculated in fresh YNB medium at OD_{600} of 0.05. Growth rates (μ) and glucose
271 consumption rate were determined by sampling cultures at 4-6 different times points (t) during the
272 exponential growth phase, starting from an OD_{600} of about 0.1 after the yeast passed the lag phase.
273 At each time point, the OD_{600} was measured, and the supernatant was collected for analysis of
274 uptake/secreted metabolite concentration. An electrochemical measurement (YSI, 2900D with

glucose starter kit YSI, 2324) was deployed to measure glucose concentration. The growth rate was determined by assuming OD_{600} changes exponentially, and the glucose uptake rate was assumed to be depleted linearly with time.

For C-limited and N-limited chemostat cultures, yeast nitrogen base (YNB) without amino acid or ammonium or phosphate (MP Biomedicals, 114029622) was used as the mineral base and supplemented with nutrients specified in Table 1 below (Shen et al., 2024). All media were filter sterilized through a 0.22μm pore filter, and then supplemented with autoclaved 5×10^{-5} v/v antifoam 204 (Sigma). To establish chemostat cultures, 2mL batch culture was inoculated into 250mL culture and grown in continuous mode at a dilution rate of $0.1h^{-1}$ in 500ml chemostats (Sixfors; Infors AG, Bottmingen, Switzerland). Cultures were stirred at 400 rpm, sparged with 12 standard liters per minute of humidified air. After over 50 h, the cell density reached steady state at $OD_{600} \approx 0.6$, and the cultures were then collected and pelleted for proteomics analysis. Label-free intensity based quantification and TMT labeled quantification were performed as described in Shen et al. (2024), including cell pellet processing, peptide preparation and labeling, peptide analysis by LC-MS, and proteomics data analysis. Peptides were searched against the reference proteome UP000199069.

Table 1. Media for yeast chemostat culture.

media (g/L)	**C limit**	**N limit**
YNB (-) AA (-) NH_4 (-) PO_4	0.700	0.700
$(NH_4)_2SO_4$	5.000	0.10
KH_2PO_4	1.000	1.000
KCl	0.000	0.000
glucose	0.800	20.000

For ^{13}C isotope tracing, RT was cultured in media with [U-$^{13}C_6$] glucose or [1,2-$^{13}C_2$] glucose (Cambridge Isotope Laboratories, Tewksbury, MA, USA) at 50% enrichment. RT was first grown

overnight in labeled media and then inoculated into fresh labeled media at OD_{600} of 0.1 to ensure steady state labeling. The cultures were allowed to grow for 10 h to reach OD_{600} of 1.

For intracellular metabolite extraction, about 2.5 mL of cell culture at OD_{600} around 1 was quickly vacuum filtered through a GVS Magna™ Nylon membrane filter with 0.45 µm pore size (Fisher Scientific, Pittsburgh, PA), quenched in 1.5 mL of ice-cold solution of 40:40:20 methanol:acetonitrile:water with 0.5% formic acid for about 1 min, and then neutralized with 132 µL of 15.8% ammonium bicarbonate. The extracts were centrifuged at 17000 x g for 10 mins, and the supernatants were analyzed by LC-MS.

Metabolites were separated by hydrophilic interaction liquid chromatography (HILIC) with using a Vanquish UHPLC system (Thermo Fisher) and Xbridge BEH Amide HILIC column (2.1 mm × 150 mm, 2.5µm particle size, 130 Å pore size). The LC method has a 25-min solvent gradient at a flow rate of 150 µL/min, with the following gradient parameters: 0 min, 90% B; 2 min, 90% B; 3 min, 75%; 7 min, 75% B; 8 min, 70%, 9 min, 70% B; 10 min, 50% B; 12 min, 50% B; 13 min, 25% B; 14 min, 25% B; 16 min, 0% B, 20.5 min, 0% B; 21 min, 90% B; 25 min, 90% B, where Solvent A was 95:5 water:acetonitrile with 20 mM ammonium hydroxide and 20 mM ammonium acetate (pH 9.4) and solvent B was acetonitrile. The autosampler temperature was 4 °C, the column temperature was 25 °C, and the injection volume was 6 µl.

MS analysis was performed on Thermo Fisher's Q Exactive Plus (QE+) Hybrid Quadrupole-Orbitrap mass spectrometer. MS scan was operated in negative mode, with the following parameters: resolution, 140,000; scan range, m/z 70-1000; normalized AGC target 3e6; ITmax, 500 ms. Other instrument parameters are: spray voltage 3000 V, sheath gas 35 (Arb), aux gas 10 (Arb), sweep gas 0.5 (Arb), ion transfer tube temperature 300 °C, vaporizer temperature 35◦C, internal mass calibration on, RF lens 50.

Raw LC/MS data were converted to mzXML format by msconvert from ProteoWizard. Peak extraction of the raw data for cells growing in unlabeled media was performed using the El-Maven software package (https://github.com/ElucidataInc/ElMaven). ^{13}C natural isotope abundance was corrected using the Accucor package (https://github.com/lparsons/accucor). A conversion factor of 0.56 grams dry weight per OD_{600} per liter was used to convert OD_{600} to a cell dry weight unit.

We employed the ^{13}C MFA procedure described previously (Gopalakrishnan and Maranas, 2015) (formulated using the elementary metabolite unit framework (Antoniewicz et al., 2007), available at https://github.com/maranasgroup/SteadyState-MFA). Briefly, a nonlinear optimization formulation was used to find a flux solution by minimizing the sum of squared differences between the simulated ^{13}C mass isotopomer distributions (as a function of fluxes) and the observed ones from both tracers (i.e., U-$^{13}C_6$-glucose and 1,2-$^{13}C_2$-glucose), as well as the glucose uptake flux. The best-fit flux solution was chosen from 200 alternative solutions with randomized initializations. Goodness-of-fit test (chi-square) and 95% confidence interval estimation were performed as described previously (Antoniewicz et al., 2006; Leighty and Antoniewicz, 2013). We then ran parsimonious FBA (pFBA, formulation in Supplementary Text 1), at the same sum-squared residual to find the flux value that equally describes the data with the lowest total flux values.

2.4 Estimation of ATP maintenance coefficients

Growth associated maintenance (GAM) and non-GAM (NGAM) were set at 167.408 mmol ATP gDW^{-1} and 1.189 mmol ATP gDW^{-1} h^{-1}, respectively, in model *iRhto*1108C's latest published version (Dinh et al., 2019). Both values were calculated using growth and uptake rate data from carbon-limited chemostat experiments (Shen et al., 2013); see Supplementary Text 1 for additional information. Upon recalculating them using the updated GSM model with the same dataset, GAM

and NGAM values increased to 251.233 mmol ATP gDW^{-1} and 1.259 mmol ATP $gDW^{-1}h^{-1}$, respectively. Because the total ATP consumption associated with translation, elongation and initiation is now directly modeled in the RBA model, the GAM value needed to be adjusted so that these costs are not double counted in the biomass equation used in the RBA model. Here, the ATP cost for translation was calculated using a comprehensive proteomics dataset (99.7% of the proteome's mass has been identified) under the same conditions as the simulation (this study). The ATP costs were estimated at 6.682 mmol ATP gDW^{-1} h^{-1} for elongation and 0.009 mmol ATP $gDW^{-1}h^{-1}$ for initiation under carbon limitation conditions. These values were derived by (a) multiplying each protein's length by the cost of elongation (i.e., 2 ATP per amino acid) (Oftadeh et al., 2021), then dividing the resulting sum by each protein's molecular weight (in g/mmol), and (b) adding 1 ATP per protein to account for initiation; these values were both scaled multiplying by the protein's measured abundances (in g/gDW) and finally summed over all produced proteins to determine the overall result. The GAM value for rtRBA was thus reduced accordingly to 244.542 mmol ATP gDW^{-1}.

2.5 Estimation of *in vivo* k_{app}

Values for k_{app} were determined via a modified version of a previously published procedure (Dinh and Maranas, 2023) summarized in Fig. 1, using proteomics data for RT. Briefly, enzyme and transporter synthesis fluxes (i.e., v_{enz}) were estimated from proteomics data (i.e., **Step B1** in Fig. 1), and every reaction *j* they can support is included in set J^P (i.e., all reactions with proteomics data for their enzymes or transporters). Enzymes with one or more subunits measured in the data were included in the set Enz^{meas}. For rtRBA and the newest scRBA version, we added **Step B1.5**, which minimizes deviations from expected flux bounds, such as those provided by MFA. To account for essential enzymes that may not have been identified or measured, the flux distribution

that minimizes the total flux through reactions outside J^P (i.e., $\sum_{j \notin J^P} v_j$) was found, while constraining growth and maximum nutrient uptake rates to experimentally determined values (i.e., **Step B2**). These essential reactions that lack proteomics data are denoted by making them members of set J_{Ess}^{NP}. All essential and measured exchange reactions are aggregated within set J_{Ess}^{Ex}. Reactions belonging to sets J_{Ess}^{NP} and J_{Ess}^{Ex} were then allowed to be part of the metabolic model. **Step B3** was next used to determine the metabolic flux distribution with the minimum sum of all metabolic fluxes (i.e., parsimony assumption invoking min $\sum v_j$) while not allowing flux through metabolic reactions not in J^P, J_{Ess}^{NP}, or J_{Ess}^{Ex}. These inferred metabolic fluxes were then divided by the enzyme concentrations to obtain k_{app} estimates. All isozymes for a reaction and all reactions catalyzed by the same enzyme were assigned the same k_{app} value. Whereas scRBA's original release used these as the final k_{app} values, our updated RBA framework uses them to help calculate how best to allocate measured and unmeasured portions of its proteome to make all necessary enzymes. The updated framework also adds 2 steps: **Step B4** minimizes the total mass of proteins not used in creating enzymes, while **Step B5** minimizes deviations from initial k_{app} estimates, to encourage as much enzyme production as possible to support reactions in J_{Ess}^{NP}. Since this added enzyme demand may change the fluxes needed by the model, **Steps B1.5** through **B3** are then rerun. The resulting proteome mass fraction devoted to each protein's sink reaction flux is set as a lower bound on the mass fraction comprised by its translation flux (i.e., "minimum protein from sink" or MPFS constraints). The full procedure and changes made are summarized in Supplementary Text 1.

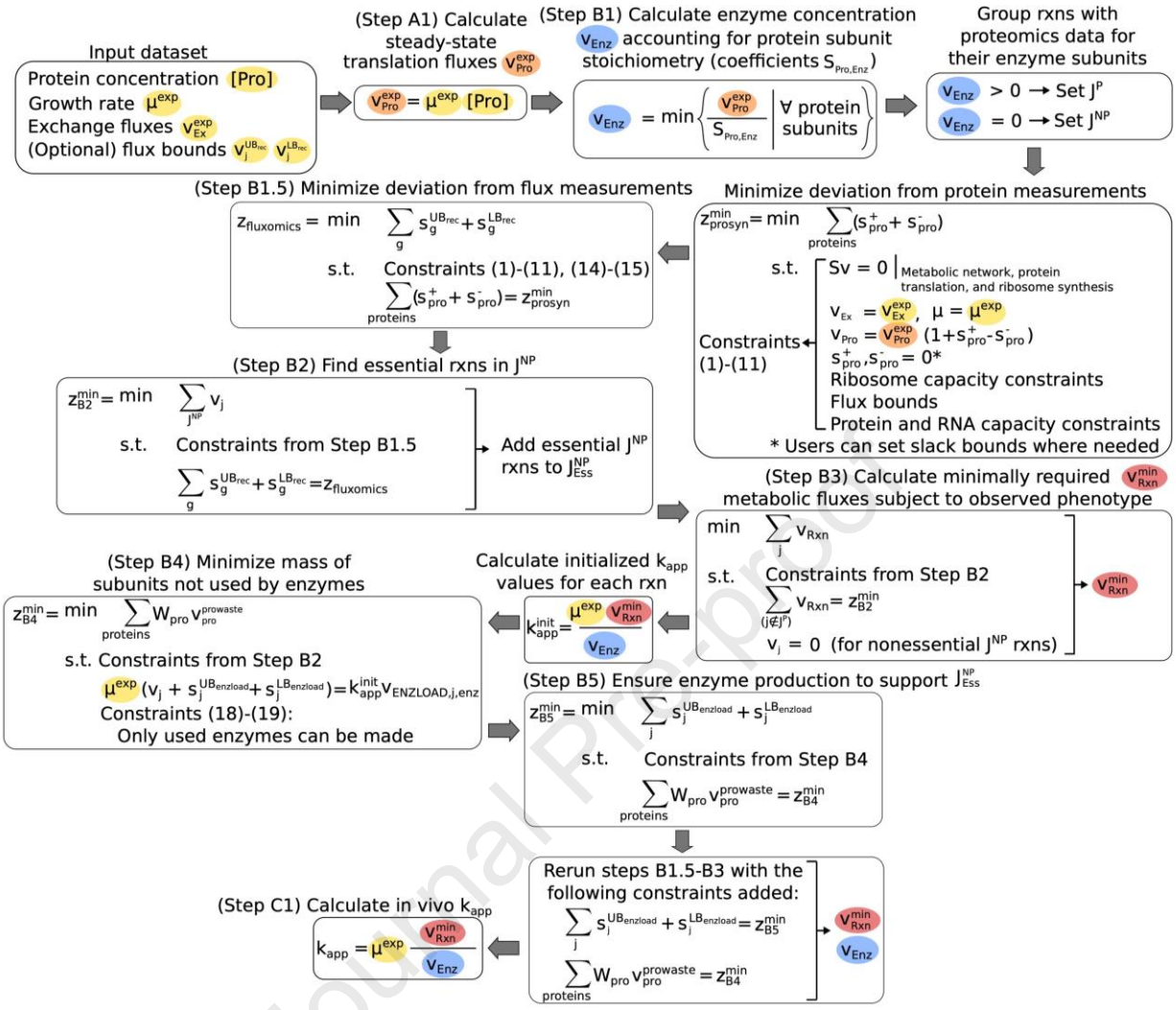

Fig. 1. Summary of the k_{app} calculation procedure for rtRBA. Colored ovals are added to distinguish key variable and parameter types: required inputs (yellow), estimated protein translation fluxes (orange), as well as metabolic fluxes (red) and enzyme synthesis fluxes (blue) used when calculating k_{app} values. Additional variable definitions: slack variables allowing a protein's translation flux to exceed or fall below its measured value (s_{pro}^{+} and s_{pro}^{-}, respectively), slack variables allowing metabolic fluxes to exceed or fall below their measured values ($s_g^{UB_{rec}}$ and $s_g^{LB_{rec}}$, respectively).

2.6 Maximal growth and theoretical yield predictions using rtRBA and FBA

For all conditions tested, the maximal growth rate and theoretical yields were assessed using an updated version of the methods developed for scRBA (Dinh and Maranas, 2023). Briefly, the model minimizes the mass of its proteome as an LP problem (i.e., RBA-LP) at a fixed growth rate; this rate becomes its new upper or lower bound on growth if the LP problem is infeasible or feasible

respectively. It then performs bisection, evaluating growth at the midpoint of its upper and lower bounds until both bounds differ by 10^{-5} h^{-1} (the tolerance criterion) or less.

Maximum theoretical yields were determined by changing RBA-LP's objective to maximizing the flux through the exchange reaction secreting the compound of interest at the observed chemostat growth rate of 0.1 h^{-1} (Li et al., 2025). The maximum yield ($Y_{p,max}^{RBA}$, in g g-glucose^{-1}) was calculated using the equation employed for scRBA:

Equation 1: $$Y_{p,max}^{RBA} = \frac{MW_p v_{p,max}^{RBA}}{MW_{glc} v_{glc}^{RBA}}$$

where MW_{glc} and MW_p are the molecular weights of glucose and the product of interest (both in g/mmol) respectively, while v_{glc}^{RBA} and $v_{p,max}^{RBA}$ are the predicted glucose uptake and maximum production rates respectively (both in mmol gDW^{-1} h^{-1}). The maximum oxygen uptake for yield calculations was determined by finding the lowest oxygen uptake that could support the maximum growth rate, as done in other bioproduction simulations (Suthers et al., 2020). For fatty alcohol yield calculations, corn steep liquor composition was adopted from another study (Wang et al., 2020). Detailed procedures for calculating experimental yields, as well as growth and uptake rates, are included in Supplementary Data 2.

2.7 Software implementation

All optimization problems involving the GSM and RBA models were formulated in COBRApy (Ebrahim et al., 2013) and the General Algebraic Modeling System (GAMS) programming language (version 42.1.0, GAMS Development Corporation), respectively. For both, IBM ILOG CPLEX (version 22.1.1.0) was used as the solver. Python 3.9.16 was used for all other scripts. RBA model input files were built as Excel spreadsheets. All scripts, inputs, and outputs are available at https://github.com/maranasgroup/rtRBA. R^2 values were calculated by squaring the output of numpy.corrcoef() in Python, which returns the Pearson correlation coefficient.

3 Results

The following sections compare *S. cerevisiae* and RT using newly elucidated metabolic fluxes and derived proteomics data, which are used to parameterize a resource balance analysis (RBA) model of RT (rtRBA). Then, rtRBA is contrasted with an updated version of the corresponding *Saccharomyces cerevisiae* model (scRBA) to pinpoint the merits of both yeasts as bioproducers.

3.1 Atom mapping model and ^{13}C metabolic flux analysis

Experimentally resolved fluxes are required for calculating k_{app} values as part of parameterizing an RBA model. *In vivo* flux distributions of RT were generated via ^{13}C tracer measurements and the application of MFA. This required building an atom mapping model by condensing stoichiometric model *iRhto*1108 into 348 metabolites and 373 tracer-relevant reactions. The glucose uptake flux was measured at 5.3 mmol gDW^{-1} h^{-1} and enforced during ^{13}C MFA calculations. The resulting MFA fluxes are listed in Supplementary Table 3, and core reactions are shown in Fig. 2. When comparing MFA fluxes to assess ATP generated from respiration and glycolysis, glycolysis contributes as much as 82% in SC but only 12% in RT (Fig. 2). This difference results from SC devoting the vast majority of its carbons to ethanol fermentation, leaving far fewer available for respiration.

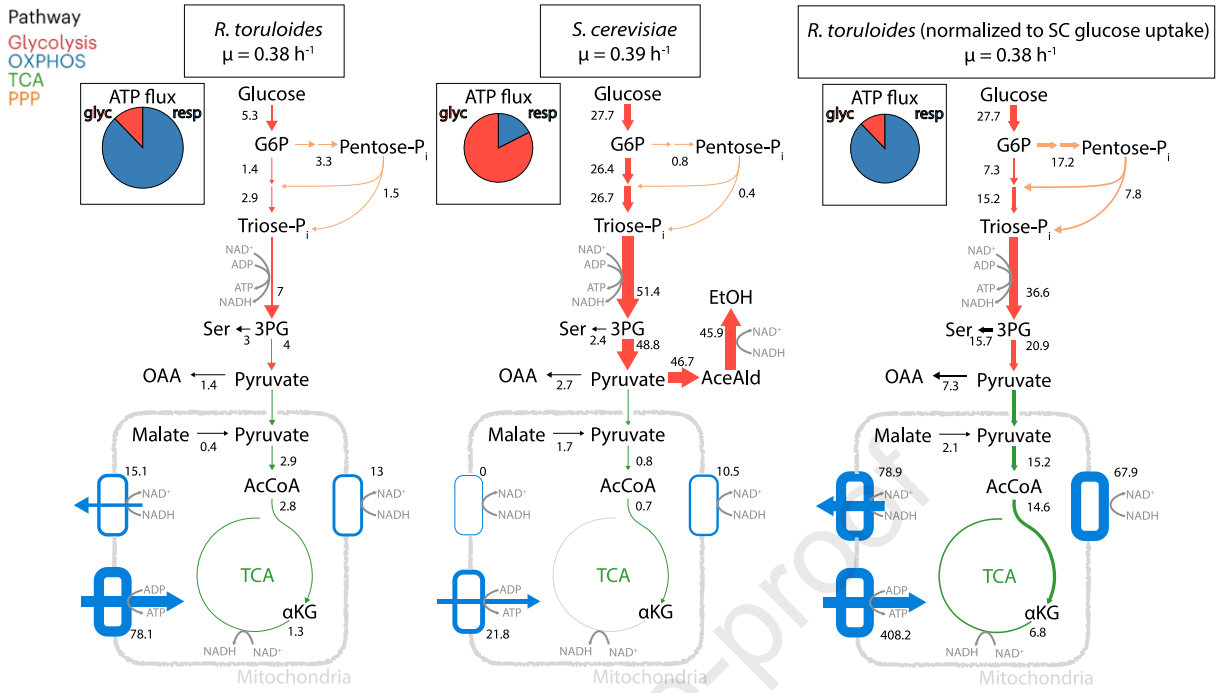

Fig. 2. Map of best-fit flux solutions determined from MFA using ^{13}C labeling data for RT (left and right) and SC [16b] (middle). For the RT normalized map (right), RT's fluxes were scaled by multiplying them by the ratio (~5.2) of SC's glucose uptake rate (27.7 mmol gDW^{-1} h^{-1}) to RT's glucose uptake rate (5.3 mmol gDW^{-1} h^{-1}). All fluxes have units of mmol gDW^{-1} h^{-1}, with line widths proportional to flux values and arrows indicating the net reaction direction. Arrows are color coded according to the pathways their reactions correspond to: glycolysis (red), oxidative phosphorylation (blue), the tricarboxylic acid cycle (TCA, green), and the pentose phosphate pathway (PPP, yellow). RT and SC were grown in aerobic batch cultures (growth rates of 0.38 and 0.39 h^{-1} respectively) on minimal (YNB) media with glucose. μ, growth rate; G6P, glucose-6-phosphate; Pi, phosphate; EtOH, ethanol; AceAld, acetaldehyde; OAA, oxalacetic acid; AcCoA, acetyl-CoA; α-KG, α-ketoglutarate; 3-phosphoglycerate, 3PG. The insets show ATP fluxes from glycolysis (glyc; specifically, the reactions PGK_c and PYK_c in both GSM models) and respiration (resp; specifically, the reactions ATPS_m and SUCOAS_m in both GSM models). The full MFA flux files are available at https://github.com/maranasgroup/yeastsMFA/tree/master/mfa/R_toruloides/result_files/batch, while a version standardized to the latest GSM model's format is available at https://github.com/maranasgroup/rtRBA/blob/main/parameterization/kapp/datasets/raw_data_files/Rabinowitz-flux.xlsx. Both files include upper and lower bound estimates of the MFA fluxes (under the "mfaUB" and "mfaLB" columns).

Despite this major difference in carbon fate and associated ATP production routes, the MFA-derived metabolic fluxes for SC vs. RT (at growth rates of 0.39 and 0.38 h^{-1}, respectively) exhibit some degree of correlation (R^2=0.26 for log-transformed fluxes in RT vs SC, Fig. 3A). RT involves somewhat higher total net fluxes (942 mmol gDW^{-1} h^{-1} vs. 701 mmol gDW^{-1} h^{-1}). When

normalizing them to their respective glucose uptake fluxes (in mmol $gDW^{-1}h^{-1}$, 27.7 and 5.3 for SC and RT, respectively) the differences are magnified even further, reflecting much more overall metabolic activity per glucose molecule in RT, as opposed to simple fermentation of most glucose to ethanol in SC (see Supplementary Figure 2). Within many individual pathways, fluxes in RT and SC strongly correlate (see Supplementary Figure 3), e.g. pentose phosphate pathway (R^2=0.97), glycolysis (R^2=0.66), and histidine metabolism (R^2=1). In contrast, some pathways are used in strikingly different ways leading to low correlations, most importantly the citric acid cycle (R^2<0.01), which runs as a full cycle in RT but effectively stops at ketoglutarate in SC.

3.2 Comparing protein abundances for SC and RT

We were able to measure 99.7% of the proteome's mass in RT. The tabulated proteomics data is available at https://github.com/maranasgroup/rtRBA/blob/main/parameterization/kapp/datasets/raw_data_files/Rabinowitz-BatchGlc-abridged.xlsx. To determine if the flux differences between organisms reflected differing protein levels, protein abundance datasets from the same conditions as the MFA datasets were compared (see Fig. 3B). The moderate correlation of the logarithmically transformed protein abundance values (i.e., R^2=0.40) for the two yeasts is not surprising given their large phylogenetic distances as SC and RT belong to different phyla (Ascomycota and Basidiomycota, respectively). Furthermore, SC and RT are facultative and obligate aerobes, respectively (Guerreiro et al., 2019; Visser et al., 1990). Thus, the reactions and enzymes they use can differ greatly, as demonstrated by the Crabtree effect's presence in SC (C. Verduyn, 1984) but absence in RT.

To assess which metabolic processes differ the most between SC and RT in their respective protein usage, each protein's gene ontology (GO) terms in SC were obtained from its UniProt entry

(in proteome UP000002311). Each protein's abundance in SC was subtracted from its homolog's abundance in RT, and the sum of those differences was calculated (Fig. 3C). GO terms with the greatest positive differences (i.e., proteins were more abundant in RT than in SC) included mitochondrial and respiratory processes (e.g., "tricarboxylic acid cycle", "cellular respiration"), which aligns with the highly differential TCA fluxes (Fig. 3A). Mitochondrial proteins comprise no more than 4.7% and 14.0% of the proteome's mass in SC and RT, respectively. The most upregulated proteins in SC compared to RT mainly had GO terms related to glucose metabolism, reflecting SC's greater glucose uptake.

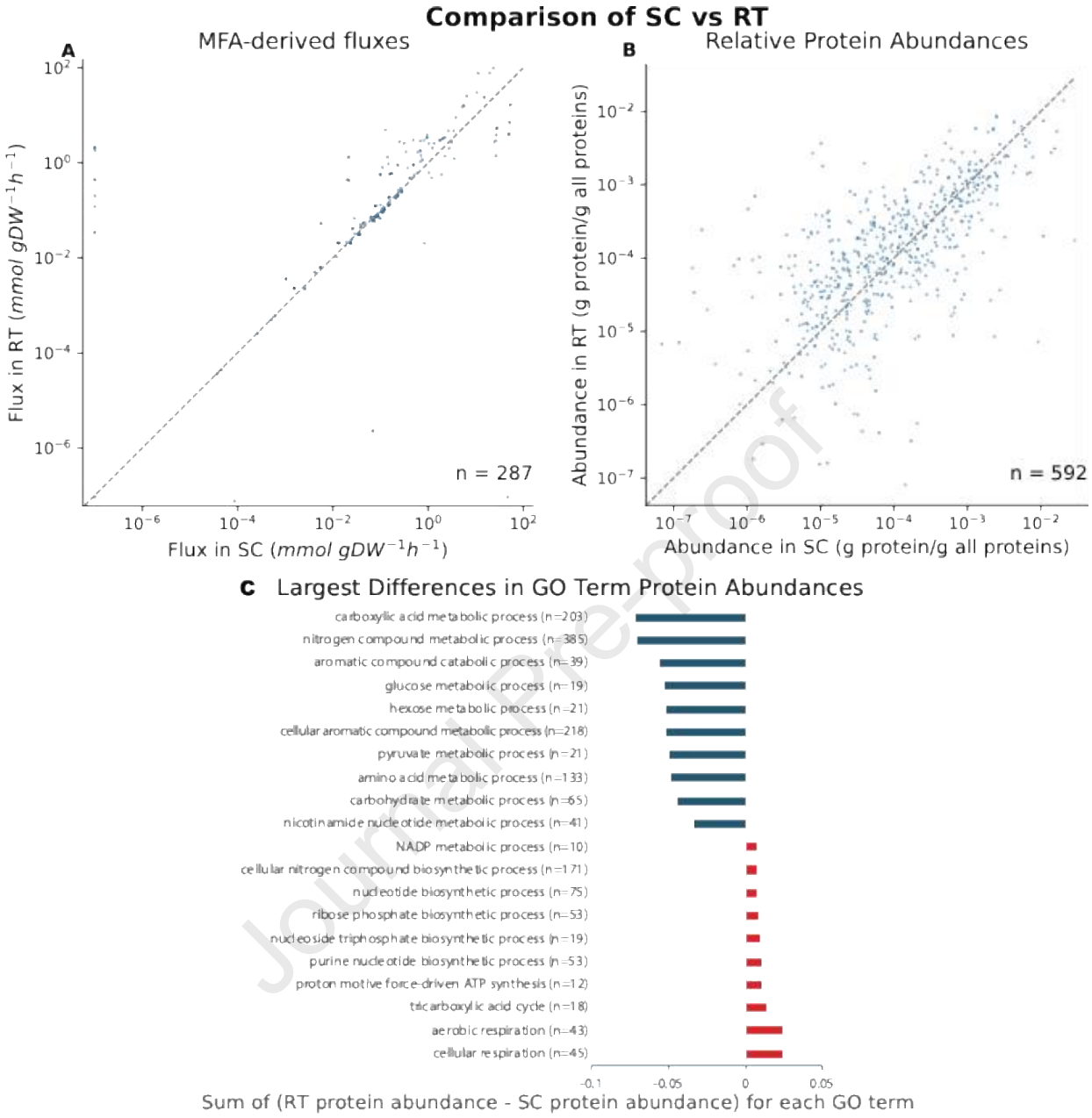

Fig. 3. Log-log plots comparing SC and RT grown in aerobic batch cultures (growth rates of 0.39 and 0.38 h^{-1} respectively) on minimal (YNB) media with glucose. To better illustrate the distribution of values, they are plotted with translucent dots which increase in intensity when overlapped, as well as a 45-degree dashed line. **(A)** Fluxes determined via ^{13}C MFA for SC (Shen et al., 2024) and RT. **(B)** Abundances of proteins found in both SC (Shen et al., 2024) and RT (this study). Each protein's homologs were identified via bidirectional BLAST searches (Dinh et al., 2019). Many proteins were expressed more in one organism than another but with no strong general preference for SC or RT. This figure's raw data are available in Supplementary Table 3. **(C)** The 10 most upregulated metabolic processes in SC (blue) and RT (red), as determined via the Gene Ontology terms associated with each protein and the total difference in protein abundance across proteins with each term. The number of proteins annotated with each term in each yeast is listed next to each term. This figure's raw data are available in Supplementary Table 2.

3.3 Comparing revised models and parsimonious FBA (pFBA) results for SC and RT

We evaluated how differences in reaction availability or stoichiometry between SC and RT impacted our MFA results, as well as the capabilities of both yeasts as bioproducers. We updated model *iRhto*1108 as it forms the starting point for the construction of model rtRBA and for ensuring more apt comparisons with the latest yeastGEM_hvd (*i.e.*, the version of *iSace*1144 updated to build scRBA, found at https://github.com/maranasgroup/scRBA/blob/main/build_model/input/GSM_iSace1144_rba.json) model. The revised RT GSM model (henceforth referred to as *iRhto*1120) has 12 new genes and 203 new reactions, primarily describing in finer detail fatty acid degradation and cofactor production. Full details are included in Supplementary Text 1. To compare *iRhto*1120 to yeastGEM_hvd on the growth media from Li et al. (2025), Flux Variability Analysis (FVA) was applied to determine the flux ranges for all reactions at the max growth rate. FVA essentially first maximizes and then minimizes the flux of each reaction separately subject to the requirement of maximum growth. This generates a hyper-rectangle inscribing all feasible flux distributions consistent with max growth. We found that 591, 219, and 693 reactions were usable in SC only, RT only, and both yeasts, respectively.

To assess whether the unique sets of usable reactions likely impact core metabolic pathways, pFBA was run (formulation in Supplementary Text 1), which determines the flux distribution with the lowest sum of absolute flux values. The reactions carrying flux in pFBA solutions exhibited a high degree of overlap between the two organisms (Table 2). A high positive correlation was observed between pFBA-predicted fluxes in both organisms (R^2=0.67, Fig. 4A), suggesting that experimentally determined differences in MFA fluxes are not driven by different pathway structures but rather differing utilizations of the same pathways. This is corroborated by the three

largest pFBA flux differences between RT and SC being in transport of reactants and products for ATP hydrolysis. The absolute values of these fluxes are much greater in RT. The next two fluxes with the largest differences are also involved in mitochondrial processes, specifically transport; this highlights mitochondrial capacity differences as a key factor distinguishing SC and RT. The full pFBA fluxes are in Supplementary Table 4. Collectively, all these increased ATP synthesis fluxes reflect the greater growth- and non-growth-associated ATP maintenance (i.e., GAM and NGAM) values in *iRhto*1120, as reported in the current work (i.e., GAM=251 mmol ATP gDW^{-1}, NGAM=1.25 mmol ATP $gDW^{-1}h^{-1}$), compared to those in yeastGEM_hvd (GAM=92 mmol ATP gDW^{-1}, NGAM=1 mmol ATP $gDW^{-1}h^{-1}$) for growth in carbon-limited chemostats (Dinh and Maranas, 2023). The higher ATP maintenance values reflect RT's larger capacity for ATP generation, possibly stemming from its greater reliance on respiration. Having higher GAM and NGAM values would necessitate higher *in silico* ATP production, as reflected by the pFBA fluxes.

Table 2. Reactions in RT and SC GSM models used in FVA and pFBA simulations under aerobic glucose conditions. Both models used the observed glucose uptake rates in carbon-limited chemostats (i.e., dilution rate of 0.1 h^{-1}) for SC (i.e., 1.03 mmol gDW^{-1} h^{-1}, Shen et al. (2024)) and RT (i.e., 1.35 mmol gDW^{-1} h^{-1}; see Supplementary Data 1).

Reaction classification	*SC only*	*RT only*	*Both*
Used in pFBA	67	0	418
Not used in pFBA	524	219	275

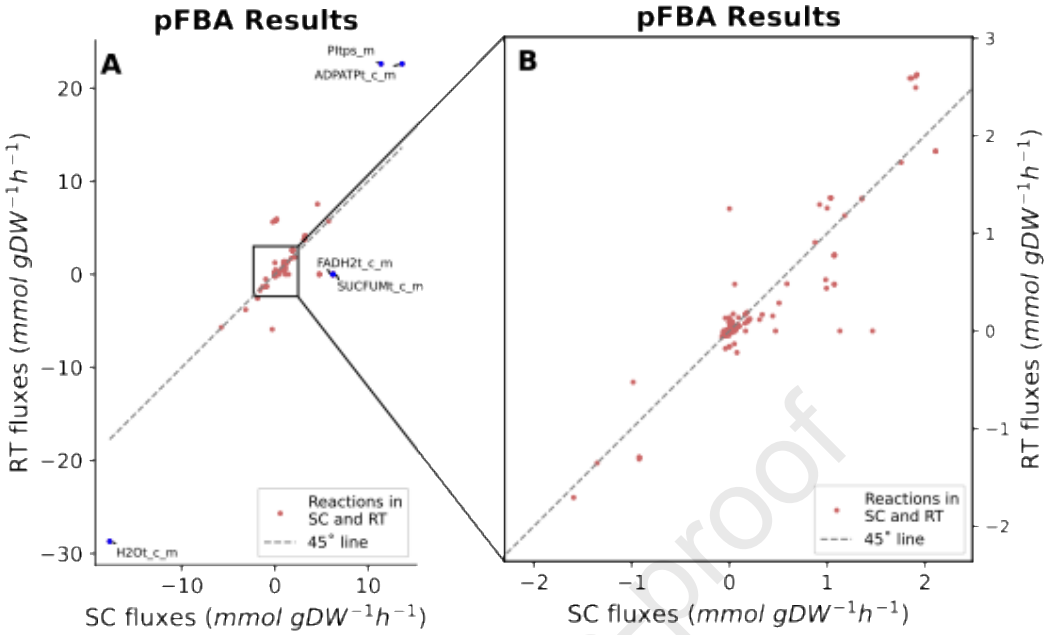

542

543 Fig. 4. **(A)** Unscaled pFBA flux values (n=397, R^2=0.67) for *iRhto*1120 (y-axis) and
544 yeastGEM_hvd (x-axis). Growth was simulated on the modified YNB media from Li et al. (2025).
545 Models were constrained to experimental growth (0.08 h^{-1} for yeastGEM_hvd, 0.1 h^{-1} for
546 *iRhto*1120) and glucose uptake rates (1.03 mmol $gDW^{-1}h^{-1}$ in SC, 1.35 mmol $gDW^{-1}h^{-1}$ in RT).
547 The 5 furthest points from the 45-degree line are mitochondrial phosphate transport (PItps_m),
548 water diffusion between the cytosol and mitochondria (H2Ot_c_m), ADP/ATP transport between
549 the cytosol and mitochondria (ADPATPt_c_m), succinate and fumarate transport between the
550 cytosol and mitochondria (SUCFUMt_c_m), and $FADH_2$ transport into the mitochondria
551 (FADH2t_c_m). **(B)** Zoomed-in version of (A), to highlight the points closer to interval [-2,3].

552 The generated MFA and proteomics data were used to parameterize model rtRBA. It includes
553 5,634 proteins, 1,266 of which serve as subunits for ribosomes and/or the model's 1,003 unique
554 enzymes. To better understand phenotypic impacts of differences in metabolic networks, and
555 determine which enzymes work faster in each yeast, k_{app} values for rtRBA were compared to their
556 counterparts in scRBA (Fig. 5). Analysis revealed that as expected, most of the assigned k_{app} values
557 (9 out of 10, not including ones for enzymes lacking proteomics data) associated with glycolysis
558 or gluconeogenesis reactions (as indicated by their subsystem in both GSM models) are higher in
559 SC. Other large discrepancies exist in amino acid metabolism, reflecting the different amino acid

compositions of both proteomes. Other factors may influence these differences too, including disparities in the prevalence or mechanism of substrate channeling between enzymes, as well as different allosteric regulator concentrations. Additional data would be required to compare such factors between SC and RT.

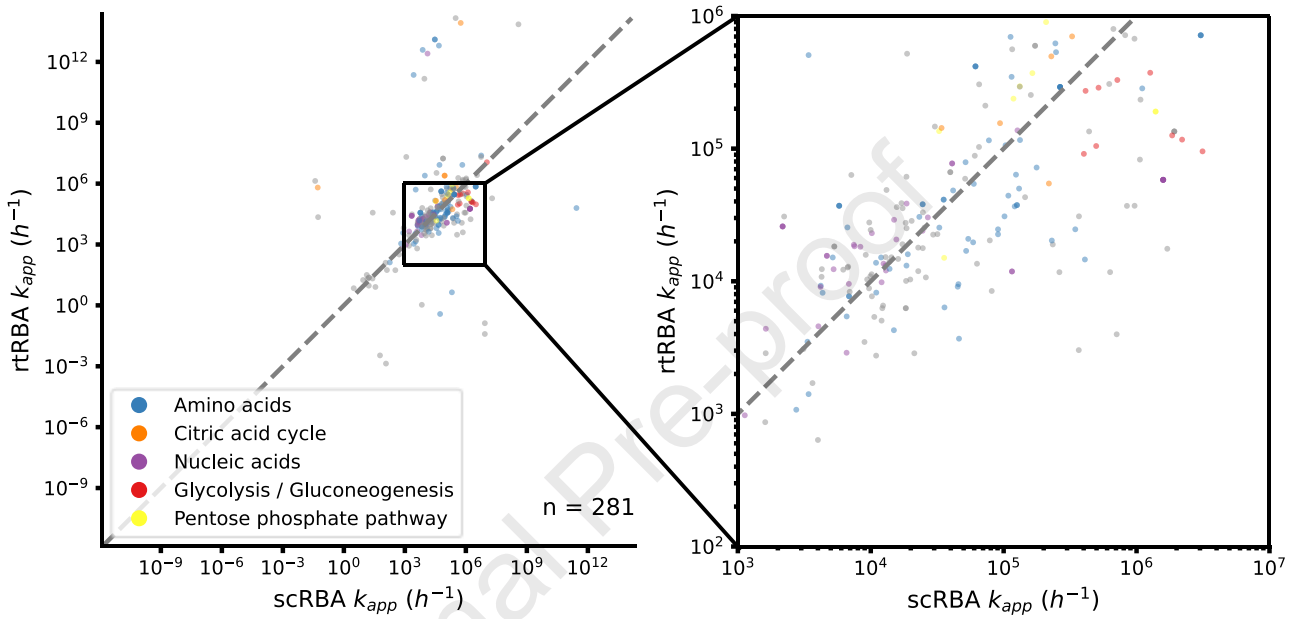

Fig. 5. k_{app} values (n=281) for SC and RT. Values were calculated using the RBA models for both organisms, constrained to experimental protein production levels and ^{13}C MFA fluxes from batch cultures. They are valid only for these conditions. For comparison, 45-degree lines are included; k_{app} values below and above it are higher in SC and RT respectively. Only k_{app} values for active reactions with experimentally detected enzyme subunits in both species were included. Each reaction's point is colored based on its subsystem. Data for this figure is available in tabular form in Supplementary Table 3.

3.4 Prediction of yields of target compounds in RT and SC

To further assess the respective biosynthetic advantages of SC and RT as bioproducers, their maximum theoretical yields (MTYs) were compared for various compounds tested using an RBA model for SC developed in a prior study (Dinh and Maranas, 2023). We calculated MTYs using RBA to obtain more realistic values for current strains, since RBA incorporates more *in vivo* data than FBA and reflects more of the biological constraints on fluxes (e.g., mitochondrial protein

capacity, limited enzyme catalytic capacity). We also calculated MTYs using FBA to determine how the proteomic constraints imposed by RBA impact yields, and guide future strain design strategies. In predicting RT's capacity for producing lipid-derived compounds, bioproduction experiments for TAGs and various fatty alcohols were replicated by adding exogenous reactions from *M. aquaeolei* VT8 Maqu_2220 (for fatty alcohols) (Fillet et al., 2015) to both models as needed. The results of these tests are summarized in Table 3. SC's fatty alcohol yields are slightly higher, though RT achieves higher yields when turning off GAM and NGAM for both (0.268 and 0.260 g stearyl alcohol/g sucrose for RT and SC, respectively), highlighting that GAM and NGAM values is a key driver for the calculated differences between them.

Table 3. Maximum predicted and *in vivo* yields (g product/g sugar) from FBA and RBA for SC and RT.

	RT			**SC**		
Product name	FBA	RBA	*In vivo*	FBA	RBA	*In vivo*
oleyl alcohol	0.222	0.221	0.027[b]	0.236	0.237	-
palmityl alcohol	0.228	0.228	0.004[b]	0.243	0.245	0.030 (Feng et al., 2015)[d]
stearyl alcohol	0.226	0.226	0.006[b]	0.241	0.243	-
TAGs[a]	0.255	0.255	0.129[c]	0.272	0.123	-

Conditions for SC yield calculations (including growth and uptake rates) were made identical to the experimental conditions used for RT, to ensure an accurate comparison.
[a] Produced using native pathways.
[b] Grown on sucrose; expresses fatty alcohol reductase from *M. aquaeolei* VT8 (Fillet et al., 2015)
[c] Yield here is from total cell content of TAG (Tiukova et al., 2019a), not just secreted amount. FBA and RBA yields are from secreted amount (i.e., the reaction EX_tag_e), and thus excludes TAGs included as biomass (less than 0.1% of secreted value).
[d] Conditions *in vivo* differ from RT; uses glucose, and fatty alcohol reductase from *Tyto alba*. For comparison, RT's yields when grown on glucose were 0.024 g/g glucose (Schultz et al., 2022).

Additional yield calculations from scRBA were also compared to rtRBA in Table 4. For most of the 20 compounds tested, the FBA yields favor RT slightly, with RT achieving 3.2% higher yields on average. The largest differences are for citramalate and polyhydroxybutyrate, for which SC achieves only 84.5% and 84.1% of RT's yields, respectively. Compared to their FBA

602 counterparts, the RBA yields for SC and RT are 50.8% and 1.6% lower on average, respectively.
603 Although rtRBA achieves 153.4% higher yields than scRBA on average, we note that SC has an
604 *in vivo* glucose uptake flux that is 423% higher. Only isobutanol had higher yields in scRBA than
605 rtRBA. FBA and RBA usually agree in predicting higher yields for RT, with L-lactate, 1,3-
606 propanediol, 2-phenylethanol, and artemisinic acid being exceptions, having greater or roughly
607 equal FBA yields in SC. Manually assessing RBA model predicted fluxes from both yeasts
608 revealed that artemisinic acid production in SC and RT involved many of the same reactions in
609 both. However, even without explicitly requiring ethanol production during yield calculations, SC
610 directs more flux towards producing pyruvate, which largely is secreted as ethanol (flux of 11.6
611 mmol gDW^{-1} h^{-1}, compared to 1.4 mmol gDW^{-1} h^{-1} for artemisinic acid secretion). Thus, it largely
612 reflects the Crabtree effect present in the MFA data used for parameterization. In the FBA version
613 of this simulation for SC, no ethanol was secreted, despite allowing the same high maximum
614 glucose and oxygen uptakes (13.2 mmol gDW^{-1} h^{-1} and 26.3 mmol gDW^{-1} h^{-1}, respectively) as
615 RBA. Since the same glucose uptake flux was used for SC and RT, we also estimated the *in vivo*
616 rates by dividing the product synthesis fluxes by the ratio of each yeast's *in vivo* and simulated
617 glucose uptake fluxes. This resulted in SC having higher rates for every product, due to its
618 significantly higher glucose uptake.

619 Table 4. Maximum predicted yields (g product/g sugar) from FBA and RBA for SC and RT, using
620 minimal media with glucose as the carbon source. Glucose uptake was set to 13.2 mmol gDW^{-1}
621 h^{-1}, as in yield calculations from Dinh and Maranas (2023). RBA rate estimates (
622 r_{RBA}, in mmol product gDW^{-1} h^{-1}) were calculated by dividing the product synthesis flux by the
623 simulated glucose uptake flux, then multiplying by each yeast's measured glucose uptake flux.
624 The higher RBA yield for each product is underlined.

	RT				**SC**			
Product name	FBA	RBA	$\frac{\text{RBA}}{\text{FBA}}$	r_{RBA}	FBA	RBA	$\frac{\text{RBA}}{\text{FBA}}$	r_{RBA}
1,3-Propanediol	0.569	<u>0.567</u>	99.7%	7.131	0.570	0.330	57.9%	21.690

2-Phenylethanol	0.356	0.350	98.4%	2.779	0.356	0.193	54.2%	7.905
3-Hydroxypropionic acid	0.787	0.778	98.9%	8.233	0.760	0.181	23.8%	10.054
p-Hydroxybenzoate	0.532	0.521	98.0%	3.700	0.522	0.185	35.4%	6.721
Artemisinic acid	0.280	0.277	99.1%	1.111	0.280	0.125	44.6%	2.663
(2R,3R)-Butanediol	0.502	0.501	99.7%	5.316	0.488	0.487	99.8%	26.989
n-Butanol	0.350	0.348	99.3%	4.509	0.349	0.274	78.5%	18.442
Citramalate	0.907	0.900	99.2%	5.633	0.767	0.306	39.9%	10.461
p-Coumaric acid	0.488	0.479	98.1%	2.856	0.486	0.212	43.6%	6.481
Hexadecanoic acid	0.303	0.299	98.6%	1.109	0.298	0.077	25.8%	1.504
Isobutanol	0.385	0.381	99.0%	1.075	0.390	0.385	98.7%	1.529
L-Lactate	0.895	0.894	99.8%	4.952	0.907	0.792	87.3%	25.947
cis,cis-Muconate	0.616	0.612	99.3%	9.598	0.614	0.283	46.1%	44.399
(2S)-Naringenin	0.470	0.461	98.1%	4.198	0.454	0.123	27.1%	10.091
Polyhydroxybutyrate	0.643	0.636	98.9%	1.624	0.541	0.207	38.3%	2.260
Reticuline	0.373	0.337	90.3%	5.601	0.348	0.068	19.5%	10.010
Resveratrol	0.394	0.387	98.3%	1.005	0.381	0.103	27.0%	1.033
Sesquiterpenes	0.313	0.309	98.8%	1.624	0.306	0.137	44.8%	2.260
Shikimate[a]	0.714	0.706	98.9%	1.164	0.712	0.334	46.9%	2.779
Styrene	0.301	0.296	98.4%	3.913	0.296	0.131	44.3%	9.579

[a] Produced using native pathways.

4 Discussion

Herein the workflow introduced for the construction of the scRBA model (Dinh and Maranas, 2023) was repurposed and generalized for the development of the rtRBA model. In the process, the workflow was streamlined and expanded to cover potentially additional organisms and growth conditions that can be modeled using RBA. For example, allowing variable ribosome composition could enable more accurate phenotype predictions, since ribosome composition can be heterogeneous and vary depending on growth conditions (Samir et al., 2018). Likewise, optionally permitting some proteins to be translated by any ribosome helps build RBA models for organisms without detailed annotations of their non-nuclear DNA. We envision that these new capabilities would accelerate the construction of RBA models for other yeasts of interest.

Moreover, the updated k_{app} calculation procedure can more directly incorporate fluxomics data, and is more robust due to apportioning all enzymes simultaneously, ensuring that each protein copy is only used by one enzyme at a time. It now aids in generating constraints to account for protein demands from non-modeled processes (e.g., transcription) without needing to aggregate the proteins involved, avoiding redundant protein production as a model's proteins are updated with new functions. These constraints ensure that the model reflects the protein costs of supporting processes that occur *in vivo* but are either not modeled (e.g., transcription or structural) or inactive during k_{app} calculations (e.g., reactions the model could have used but did not). The former includes proteins not involved in transport or metabolic processes, which comprise up to 50% of RT's proteome by mass, according to this study's proteomics data, and 45% in scRBA (Dinh and Maranas, 2023); the latter category was not explicitly accounted for in scRBA's original version. By limiting translation instead of protein sink reactions, these constraints allow use of *in vivo* reserve enzyme capacity. They can also be deactivated by users for individual proteins when they interfere with gene essentiality predictions or other simulations, so the proteome's composition is affected by knocking out specific genes while retaining contributions from the nonmodeled functions of others.

The calculated k_{app} values allow the model to account for *in vivo* phenomena (e.g., substrate channeling, allosteric regulation) impacting enzyme catalysis. Since they are from a wild-type strain found in soil (Coradetti et al., 2018), new strains designed to maximize yields may have different cellular conditions (e.g., allosteric regulator concentrations) that RT's enzymes did not evolve to function optimally within. Thus, the wild-type k_{app} values are expected to be higher on average than those of engineered strains, except in cases where those strains have redesigned versions of native enzymes. This is corroborated by a prior study finding that SC's enzymes

generally have higher k_{app} values than k_{cat} values (Dinh and Maranas, 2023), suggesting it evolved processes that generally improve enzyme performance and that similar improvements may exist in other yeasts. Therefore, despite having k_{app} values for only one condition, we expect rtRBA's MTY predictions to match or exceed *in vivo* yields under the conditions tested.

RT supports higher net MFA-derived fluxes overall (i.e., 942 mmol gDW^{-1} h^{-1} vs. 701 mmol gDW^{-1} h^{-1}) than SC despite its lower glucose uptake rate. This seeming paradox can be explained by its greater reliance on respiration for ATP generation, which produces more ATP per mole of uptaken glucose (Shen et al., 2024). Both organisms use many of the same reactions to grow, with *in vivo* and *in silico* fluxes tracking similar trends aside from a few notable outliers mainly in ATP generation. Protein abundances are in closer agreement between the two yeasts compared to MFA fluxes. Many factors could explain this, since both yeasts are from different phyla; homologous enzymes may have evolved with different catalytic efficiencies, while still being produced at similar levels due to conserved regulatory mechanisms. The proteome discrepancies propagate to the calculated k_{app} values. Additional causes for the apparent kinetic parameter differences include possibly differing substrate channeling and allosteric regulation.

For most bioproducts, RT had higher max theoretical yields than SC, despite a much lower *in vivo* glucose uptake flux. Thus, increasing RT's glucose uptake flux could in principle further boost productivity. Its higher FBA yields for most products – especially citramalate and polyhydroxybutyrate – suggest it may have stoichiometric advantages, such as additional reactions allowing more efficient biomass production. RBA yields suggest more substantial proteomic advantages for RT in general, as well as for products that had higher or nearly identical FBA yields for SC. These include glycols such as 1,3-Propanediol and n-Butanol, as well as artemisinic acid. As detailed prior, SC and RT are facultative aerobes, meaning RT can specialize more in the

aerobic conditions used for our MTY calculations. Only the RBA representation was able to replicate the Crabtree effect in SC, leading to substantial ethanol secretion at the expense of product yields. Redirecting flux away from ethanol production has been used *in vivo* to improve yields of artemisinic acid precursors from SC (Shiba et al., 2007), though ethanol was not secreted when maximizing artemisinic acid production in scRBA's original release. This changed in the current work, suggesting that the updated RBA procedure more robustly reflects SC's metabolic programming. As observed *in vivo*, SC achieves slightly higher fatty alcohol yields, except when ATP maintenance requirements are removed. Further investigation into *in vivo* ATP usage – especially for nonmetabolic processes captured by GAM and NGAM – may yield more precise estimates to guide future modeling efforts revealing opportunities for improving yields in both yeasts.

5 Glossary

Term	Definition
RT	*Rhodotorula toruloides* IFO0880 (now called NBRC 0880)
SC	*Saccharomyces cerevisiae*
FBA	Flux Balance Analysis
RBA	Resource Balance Analysis
pFBA	Parsimonious Flux Balance Analysis
MFA	Metabolic Flux Analysis
k_{app}	*in vivo* apparent turnover number

6 Declaration of competing interest

There are no conflicts to declare.

7 CRediT author statement

Eric J. Mooney: Conceptualization, Methodology, Software, Formal analysis, Investigation, Data curation, Writing – Original Draft. **Patrick F. Suthers**: Writing – review & editing. **Wheaton L. Schroeder**: Writing – review & editing. **Hoang V. Dinh**: Conceptualization, Methodology, Software, Formal analysis, Investigation, Data curation, Writing – review & editing. **Xi Li**: Investigation, Writing – review & editing. **Tianxia Xiao**: Investigation. **Catherine M. Call**: Investigation. **Heide Baron**: Investigation. **Arjuna M. Subramanian**: Investigation. **Daniel R. Weilandt**: Investigation. **Felix C. Keber**: Investigation. **Martin Wühr**: Resources, Supervision. **Yihui Shen**: Conceptualization, Investigation, Writing – review & editing. **Joshua D. Rabinowitz**: Conceptualization, Resources, Supervision, Funding acquisition, Writing – review & editing. **Costas D. Maranas**: Conceptualization, Investigation, Writing – Review & Editing, Resources, Supervision, Funding acquisition.

8 Acknowledgements

This work was funded by the DOE Center for Advanced Bioenergy and Bioproducts Innovation (U.S. Department of Energy, Office of Science, Biological and Environmental Research Program under Award Number DE-SC0018420). Any opinions, findings, and conclusions or recommendations expressed in this publication are those of the author(s) and do not necessarily reflect the views of the U.S. Department of Energy. Computations for this research were performed on the Pennsylvania State University's Roar Collab supercomputer. The authors of this work recognize the Penn State Institute for Computational and Data Sciences (RRID:SCR_025154) for providing access to computational research infrastructure within the Roar Core Facility (RRID: SCR_026424).

9 Supplementary Data

Supplementary Data 1.

Supplementary Data 2.

Supplementary Figure 1.

Supplementary Figure 2.

Supplementary Figure 3.

Supplementary Table 1.

Supplementary Table 2.

Supplementary Table 3.

Supplementary Table 4.

Supplementary Text 1.

10 References

Altschul, S. F., Gish, W., Miller, W., Myers, E. W., Lipman, D. J., 1990. Basic local alignment search tool. J Mol Biol. 215**,** 403-10.

Antoniewicz, M. R., Kelleher, J. K., Stephanopoulos, G., 2006. Determination of confidence intervals of metabolic fluxes estimated from stable isotope measurements. Metabolic Engineering. 8**,** 324-337.

Antoniewicz, M. R., Kelleher, J. K., Stephanopoulos, G., 2007. Elementary metabolite units (EMU): A novel framework for modeling isotopic distributions. Metabolic Engineering. 9**,** 68-86.

Bandhu, S., Srivastava, A., Ghosh, D., Chaudhuri, T. K., 2020. Yeast Single Cell Oils from Bioresources: Current Developments in Production and Applications. Current Sustainable/Renewable Energy Reports. 7**,** 109-120.

Burgard, A., Burk, M. J., Osterhout, R., Van Dien, S., Yim, H., 2016. Development of a commercial scale process for production of 1,4-butanediol from sugar. Curr Opin Biotechnol. 42**,** 118-125.

Burgard, A. P., Pharkya, P., Maranas, C. D., 2003. Optknock: A bilevel programming framework for identifying gene knockout strategies for microbial strain optimization. Biotechnol Bioeng. 84**,** 647-657.

C. Verduyn, T. P. L. Z., J.P. van Dijken, W.A. Scheffers, 1984. Continuous measurement of ethanol production by aerobic yeast suspensions with an enzyme electrode.

Caspi, R., Billington, R., Ferrer, L., Foerster, H., Fulcher, C. A., Keseler, I. M., Kothari, A., Krummenacker, M., Latendresse, M., Mueller, L. A., Ong, Q., Paley, S., Subhraveti, P., Weaver, D. S., Karp, P. D., 2016. The MetaCyc database of metabolic pathways and

752 enzymes and the BioCyc collection of pathway/genome databases. Nucleic Acids Res. 44**,**
753 D471-80.
754 Consortium, R. N., 2021. RNAcentral 2021: secondary structure integration, improved sequence
755 search and new member databases. Nucleic Acids Res. 49**,** D212-D220.
756 Coradetti, S. T., Pinel, D., Geiselman, G. M., Ito, M., Mondo, S. J., Reilly, M. C., Cheng, Y. F.,
757 Bauer, S., Grigoriev, I. V., Gladden, J. M., Simmons, B. A., Brem, R. B., Arkin, A. P.,
758 Skerker, J. M., 2018. Functional genomics of lipid metabolism in the oleaginous yeast
759 Rhodosporidium toruloides. Elife. 7.
760 Dinh, H. V., Maranas, C. D., 2023. Evaluating proteome allocation of Saccharomyces cerevisiae
761 phenotypes with resource balance analysis. Metab Eng. 77**,** 242-255.
762 Dinh, H. V., Suthers, P. F., Chan, S. H. J., Shen, Y., Xiao, T., Deewan, A., Jagtap, S. S., Zhao, H.,
763 Rao, C. V., Rabinowitz, J. D., Maranas, C. D., 2019. A comprehensive genome-scale
764 model for Rhodosporidium toruloides IFO0880 accounting for functional genomics and
765 phenotypic data. Metab Eng Commun. 9**,** e00101.
766 Ebrahim, A., Lerman, J. A., Palsson, B. O., Hyduke, D. R., 2013. COBRApy: COnstraints-Based
767 Reconstruction and Analysis for Python. BMC Systems Biology. 7**,** 74.
768 Feng, X., Lian, J., Zhao, H., 2015. Metabolic engineering of Saccharomyces cerevisiae to improve
769 1-hexadecanol production. Metabolic Engineering. 27**,** 10-19.
770 Fillet, S., Gibert, J., Suárez, B., Lara, A., Ronchel, C., Adrio, J. L., 2015. Fatty alcohols production
771 by oleaginous yeast. Journal of Industrial Microbiology and Biotechnology. 42**,** 1463-
772 1472.
773 Goelzer, A., Fromion, V., Scorletti, G., 2011. Cell design in bacteria as a convex optimization
774 problem. Automatica. 47**,** 1210-1218.
775 Goelzer, A., Muntel, J., Chubukov, V., Jules, M., Prestel, E., Nölker, R., Mariadassou, M.,
776 Aymerich, S., Hecker, M., Noirot, P., Becher, D., Fromion, V., 2015. Quantitative
777 prediction of genome-wide resource allocation in bacteria. Metabolic Engineering. 32**,**
778 232-243.
779 Gopalakrishnan, S., Maranas, C. D., 2015. 13C metabolic flux analysis at a genome-scale.
780 Metabolic Engineering. 32**,** 12-22.
781 Gu, C., Kim, G. B., Kim, W. J., Kim, H. U., Lee, S. Y., 2019. Current status and applications of
782 genome-scale metabolic models. Genome Biology. 20**,** 121.
783 Guerreiro, F., Constantino, A., Lima-Costa, E., Raposo, S., 2019. A new combined approach to
784 improved lipid production using a strictly aerobic and oleaginous yeast. Eng Life Sci. 19**,**
785 47-56.
786 IEA, World Energy Balances: Overview. 2021.
787 Kim, J., Coradetti, S. T., Kim, Y. M., Gao, Y., Yaegashi, J., Zucker, J. D., Munoz, N., Zink, E.
788 M., Burnum-Johnson, K. E., Baker, S. E., Simmons, B. A., Skerker, J. M., Gladden, J. M.,
789 Magnuson, J. K., 2020. Multi-Omics Driven Metabolic Network Reconstruction and
790 Analysis of Lignocellulosic Carbon Utilization in Rhodosporidium toruloides. Front
791 Bioeng Biotechnol. 8**,** 612832.
792 Kim, M., Park, B. G., Kim, E.-J., Kim, J., Kim, B.-G., 2019. In silico identification of metabolic
793 engineering strategies for improved lipid production in Yarrowia lipolytica by genome-
794 scale metabolic modeling. Biotechnology for Biofuels. 12**,** 187.
795 Koh, H. G., Yook, S., Oh, H., Rao, C. V., Jin, Y. S., 2024. Toward rapid and efficient utilization
796 of nonconventional substrates by nonconventional yeast strains. Curr Opin Biotechnol. 85**,**
797 103059.

Leighty, R. W., Antoniewicz, M. R., 2013. COMPLETE-MFA: Complementary parallel labeling experiments technique for metabolic flux analysis. Metabolic Engineering. 20**,** 49-55.

Levi, P. G., Cullen, J. M., 2018. Mapping Global Flows of Chemicals: From Fossil Fuel Feedstocks to Chemical Products. Environmental Science & Technology. 52**,** 1725-1734.

Li, H., Alper, H. S., 2016. Enabling xylose utilization in Yarrowia lipolytica for lipid production. Biotechnology Journal. 11**,** 1230-1240.

Li, X., Weilandt, D. R., Keber, F. C., Subramanian, A. M., Loynes, S. R., Rao, C. V., Shen, Y., Wuhr, M., Rabinowitz, J. D., 2025. Lipid accumulation in nitrogen and phosphorus-limited yeast is caused by less growth-related dilution. Metab Eng. 93**,** 60-72.

Liu, Z., Moradi, H., Shi, S., Darvishi, F., 2021. Yeasts as microbial cell factories for sustainable production of biofuels. Renewable and Sustainable Energy Reviews. 143**,** 110907.

Mahadevan, R., Schilling, C. H. H., 2003. The effects of alternate optimal solutions in constraint-based genome-scale metabolic models. Metabolic Engineering. 5**,** 264-276.

O'Brien, E. J., Lerman, J. A., Chang, R. L., Hyduke, D. R., Palsson, B. Ø., 2013. Genome ‐ scale models of metabolism and gene expression extend and refine growth phenotype prediction. Mol Syst Biol. 9**,** 693.

Oftadeh, O., Salvy, P., Masid, M., Curvat, M., Miskovic, L., Hatzimanikatis, V., 2021. A genome-scale metabolic model of *Saccharomyces cerevisiae* that integrates expression constraints and reaction thermodynamics. Nat Commun. 12**,** 4790.

Palmer, J. D., Brigham, C. J., 2016. Feasibility of triacylglycerol production for biodiesel, utilizing Rhodococcus opacus as a biocatalyst and fishery waste as feedstock. Renewable and Sustainable Energy Reviews. 56**,** 922-928.

Rekena, A., Pinheiro, M. J., Bonturi, N., Belouah, I., Tammekivi, E., Herodes, K., Kerkhoven, E. J., Lahtvee, P. J., 2023. Genome-scale metabolic modeling reveals metabolic trade-offs associated with lipid production in Rhodotorula toruloides. PLoS Comput Biol. 19**,** e1011009.

Ribeiro, R. M. M. G. P., Picão, B. W., Gonçalves, D. O., Scontri, M., Mazziero, V. T., Mussagy, C. U., Raghavan, V., Astudillo-Castro, C., Córdova, A., Cerri, M. O., Tambourgi, E. B., 2023. Synergistic Effects of Stirring and Aeration Rate on Carotenoid Production in Yeast Rhodotorula toruloides CCT 7815 Envisioning Their Application as Soap Additives. Fermentation. 9.

Samir, P., Browne, C. M., Rahul, Sun, M., Shen, B., Li, W., Frank, J., Link, A. J., 2018. Identification of Changing Ribosome Protein Compositions using Mass Spectrometry. PROTEOMICS. 18**,** 1800217.

Sànchez Nogué, V., Karhumaa, K., 2015. Xylose fermentation as a challenge for commercialization of lignocellulosic fuels and chemicals. Biotechnology Letters. 37**,** 761-772.

Schroeder, W. L., Suthers, P. F., Willis, T. C., Mooney, E. J., Maranas, C. D., 2024. Current State, Challenges, and Opportunities in Genome-Scale Resource Allocation Models: A Mathematical Perspective. Metabolites. 14**,** 365.

Schultz, J. C., Mishra, S., Gaither, E., Mejia, A., Dinh, H., Maranas, C., Zhao, H., 2022. Metabolic engineering of Rhodotorula toruloides IFO0880 improves C16 and C18 fatty alcohol production from synthetic media. Microb Cell Fact. 21**,** 26.

Shen, H., Gong, Z., Yang, X., Jin, G., Bai, F., Zhao, Z. K., 2013. Kinetics of continuous cultivation of the oleaginous yeast Rhodosporidium toruloides. J Biotechnol. 168**,** 85-89.

Shen, Y., Dinh, H. V., Cruz, E. R., Chen, Z., Bartman, C. R., Xiao, T., Call, C. M., Ryseck, R.-P., Pratas, J., Weilandt, D., Baron, H., Subramanian, A., Fatma, Z., Wu, Z.-Y., Dwaraknath, S., Hendry, J. I., Tran, V. G., Yang, L., Yoshikuni, Y., Zhao, H., Maranas, C. D., Wühr, M., Rabinowitz, J. D., 2024. Mitochondrial ATP generation is more proteome efficient than glycolysis. Nature Chemical Biology.

Shiba, Y., Paradise, E. M., Kirby, J., Ro, D.-K., Keasling, J. D., 2007. Engineering of the pyruvate dehydrogenase bypass in Saccharomyces cerevisiae for high-level production of isoprenoids. Metabolic Engineering. 9**,** 160-168.

Subash Chandra Bose, K., Shah, M. I., Krishna, J., Sankaranarayanan, M., 2023. Genome-scale metabolic model analysis of Pichia pastoris for enhancing the production of S-adenosyl-l-methionine. Bioprocess and Biosystems Engineering. 46**,** 1471-1482.

Suthers, P. F., Dinh, H. V., Fatma, Z., Shen, Y., Chan, S. H. J., Rabinowitz, J. D., Zhao, H., Maranas, C. D., 2020. Genome-scale metabolic reconstruction of the non-model yeast Issatchenkia orientalis SD108 and its application to organic acids production. Metab Eng Commun. 11**,** e00148.

Thiele, I., Palsson, B. Ø., 2010. A protocol for generating a high-quality genome-scale metabolic reconstruction. Nature Protocols. 5**,** 93-121.

Tiukova, I. A., Brandenburg, J., Blomqvist, J., Sampels, S., Mikkelsen, N., Skaugen, M., Arntzen, M. O., Nielsen, J., Sandgren, M., Kerkhoven, E. J., 2019a. Proteome analysis of xylose metabolism in Rhodotorula toruloides during lipid production. Biotechnol Biofuels. 12**,** 137.

Tiukova, I. A., Prigent, S., Nielsen, J., Sandgren, M., Kerkhoven, E. J., 2019b. Genome-scale model of Rhodotorula toruloides metabolism. Biotechnol Bioeng. 116**,** 3396-3408.

Trinh, C. T., Unrean, P., Srienc, F., 2008. Minimal *Escherichia coli* Cell for the Most Efficient Production of Ethanol from Hexoses and Pentoses. Applied and Environmental Microbiology. 74**,** 3634-3643.

Visser, W., Scheffers, W. A., Batenburg-van der Vegte, W. H., van Dijken, J. P., 1990. Oxygen requirements of yeasts. Applied and Environmental Microbiology. 56**,** 3785-3792.

Wang, G., Zhang, P., Shi, B., Zhao, T., Yin, H., Qiao, C., 2020. Effects of Corn Steep Liquor on ß-poly(L-malic Acid) Production in Aureobasidium Melanogenum.

Xie, Z. T., Mi, B. Q., Lu, Y. J., Chen, M. T., Ye, Z. W., 2024. Research progress on carotenoid production by Rhodosporidium toruloides. Appl Microbiol Biotechnol. 108**,** 7.

Zainuddin, M. F., Fai, C. K., Ariff, A. B., Rios-Solis, L., Halim, M., 2021. Current Pretreatment/Cell Disruption and Extraction Methods Used to Improve Intracellular Lipid Recovery from Oleaginous Yeasts. Microorganisms. 9**,** 251.

Zhang, Y., Peng, J., Zhao, H., Shi, S., 2021. Engineering oleaginous yeast Rhodotorula toruloides for overproduction of fatty acid ethyl esters. Biotechnol Biofuels. 14**,** 115.

Zhu, Z., Zhang, S., Liu, H., Shen, H., Lin, X., Yang, F., Zhou, Y. J., Jin, G., Ye, M., Zou, H., Zhao, Z. K., 2012. A multi-omic map of the lipid-producing yeast Rhodosporidium toruloides. Nat Commun. 3**,** 1112.

Highlights

A resource balance analysis model for *Rhodotorula toruloides* was created.

Generated proteomics and fluxomics data for *R. toruloides*.

R. toruloides consumes 19% as much glucose as *Saccharomyces cerevisiae.*

R. toruloides allocates more proteome mass to respiration than *S. cerevisiae*.

Maximum theoretical yields were predicted for 24 compounds in *R. toruloides.*